(Received 29 May 2025, Accepted 27 August 2025, Scheduled 6 September 2025)

Analysis of a Novel Flux Switching Consequent Pole Pseudo-Direct-Drive Machine in Multi-Physics Field

Kunwei Hong[1], Zhangwu Huang[2], and Libing Jing[3,*]

[1]State Grid Fujian Electric Power Co., Ltd., Hua'an County Power Supply Company, China
[2]State Grid Fujian Electric Power Co., Ltd., Ultra High Voltage Branch, China
[3]College of Electrical Engineering and New Energy, China Three Gorges University, Yichang 443002, China

ABSTRACT: Pseudo-direct-drive (PDD) machine is a new type of permanent magnet machine with high torque density and efficiency. PDD with consequent poles can reduce the influence of outer PM on electromagnetic torque, but it has the disadvantage of high eddy current loss which will limit the range of speed. By transferring PMs from high-speed rotor to low-speed rotor, the eddy current loss in PMs is reduced, and the high-speed rotor is more robust. In this paper, a flux-switching consequent pole PDD (CP-PDD) machine is built. After optimization through a multi-objective genetic algorithm, the superiority of the proposed machine to regular CP-PDD is demonstrated by comparing it through the finite element method. The output torque of the proposed machine is greatly affected by the direct drive torque. A prototype is built and tested to verify the proposed machine. Results show that the proposed machine is more suitable for high-speed operation due to the reduction of loss and robustness of the high-speed rotor. The working temperature of the proposed machine is analyzed, and there is almost no irreversible demagnetization.

1. INTRODUCTION

Pseudo-direct-drive (PDD) machine plays an important role in many fields with performance requirements of low-speed high torque, high torque density, and high efficiency, such as medicine, petrochemical, aerospace, and other fields. Based on magnetic field modulation theory [1–3], a PDD machine is composed of a permanent magnet synchronous motor (PMSM) and a magnetic gear (MG). In PDD machines, PMSM mainly generates electromagnetic (EM) torque. MG is responsible for torque transmission, and the permanent magnet (PM) of the stator causes a small amount of flux-reversal torque. PDD machine is a type of flux-modulation machine, and its each component can constitute the elements of flux-modulation. The modulation ring of a PDD machine acts as a flux filter and outputs torque.

Conventional mechanical gear has the drawback of loud noise and friction. It is easy to lead to increased abrasion and the possibility of serious failure consequences. However, MG has the natural advantage of not needing lubrication or regular maintenance [4, 5]. It works with the protection of out-of-step and overload, and the no-maintenance life of MG is more than 10 years [6]. A coaxial MG with double-layer PMs and spoke structure is proposed with better performance [7].

A multi-pole permanent magnet array of PDD is attached to the stator tooth of the machine. By coupling the inner rotor of the permanent magnet synchronous machine (PMSM) and the high-speed rotor of MG, EM torque can be transmitted and output on the outer rotor [8, 9]. Compared with the conventional radially series-connected magnetic-geared machine (RSMGM) [10], only two air gaps make the structure of PDD more compact and simpler [11]. Thus, a lower demand for machining accuracy and process requirements is needed, but the torque density of the PDD machine is relatively lower than the RSMGM of the same size. However, conventional PDD has the disadvantage that the PMs fixed on the stator teeth have a large resistance to the flux caused by windings, reducing the EM torque. Thus, a consequent pole PDD (CP-PDD) comes into being with embedded PMs in slot opening which will not influence the flux of windings [12]. Thus, the back electromotive force (EMF) and EM torque will be increased.

The drawback of CP-PDD is the large flux leakage of PMs in slot opening which will influence the utilization ratio of PM and electromagnetic performances of the machine. By adding auxiliary teeth outside the consequent pole PMs, the structure of PMs can be more stable, and the problem of flux leakage can be improved [13]. On this basis, a machine with Halbach consequent-pole in the stator opening is proposed, which verifies the superiority of Halbach consequent-pole compared with conventional consequent pole due to the reduction of flux leakage [14]. Besides, the size of the end-winding has a great influence on the torque density of the PDD machine. Therefore, a concentrated-winding split-tooth VPDD (ST-VPDD) is proposed [15]. The split-tooth VPDD can reduce the size of the end-winding and output higher torque density. Recently, a novel flux-switching magnetic gear (FSMG) has been proposed to adapt to high-speed operation [16]. The eddy current loss of the machine at higher speed is reduced, and high-speed rotor has better robustness. By applying the properties and structure of FSMG in a CP-PDD machine, the good performance of FSMG at higher speed can be inherited, reducing loss and in-

* Corresponding author: Libing Jing (jinglibing163@163.com).

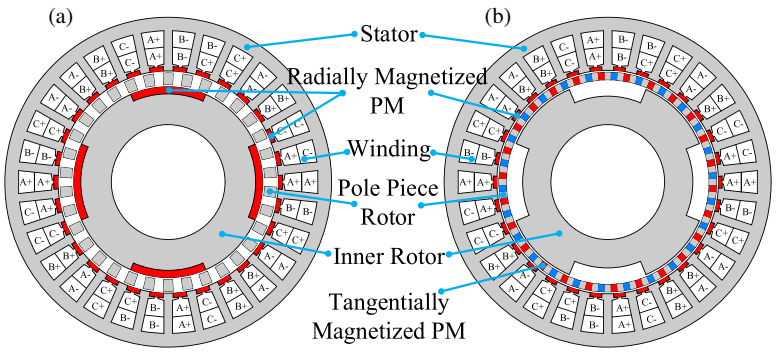

FIGURE 1. Topology comparison. (a) Conventional CP-PDD. (b) Proposed FSCP-PDD.

creasing efficiency. Direct-drive torque has a great influence on the output torque of the machine. The machine can effectively reduce loss and improve the robustness of the rotor, which is more suitable for high speed operation.

With CP-PDD as a typical electromechanical equipment, its performance depends on the complex coupling relationship among the electromagnetic field, mechanical structure, and thermal characteristics. To deeply verify the performance of the machine, multi-physical field analysis is necessary. Losses of the electromagnetic field raise the material temperature of the machine, and the temperature rise affects the performance of PMs and windings as well, thus forming a bidirectional coupling [17–19]. The machine is subjected to various loads and incentives, requiring its structure to have sufficient mechanical strength and fatigue performance [20, 21].

A flux-switching CP-PDD (FSCP-PDD) machine is proposed in this paper. The structure of this paper is as follows. In Section 2, the topology and operation principle of FSCP-PDD are described. Optimization of the machine is carried out in Section 3. Comparison of electromagnetic performances, loss, and mechanical strength between the proposed machine and conventional CP-PDD machine is carried out through the finite element method (FEM) in Section 4. The temperature of the proposed machine is analyzed in Section 4 as well. A prototype is built and tested in Section 5 to verify the proposed machine. Finally, conclusion is shown in Section 6.

2. TOPOLOGY AND OPERATION PRINCIPLE

2.1. Topology

As shown in Fig. 1, the key distinction between FSCP-PDD and conventional CP-PDD is the position of inner PMs. The consequent pole PM of CP-PDD in the inner rotor is radially magnetized. In contrast, the tangentially alternating magnetized PMs of FSCP-PDD are located in the interspace of pole pieces. There are two rotors in FSCP-PDD. The inner rotor of the proposed machine consists of an iron core of salient structure with mechanical strong strength, which is suitable for driving in high-speed regions. With the radially magnetized consequent pole PMs in each slot opening, the pole-pair number of outer PMs P_o equals the number of stator teeth and slots. The double-layer fractional slot winding is applied in the slots. With the winding step of 4 and pole-pair number of 4, the winding factor is 0.951. The pole-pair number of winding equals the pole-pair number of inner rotor P_i. In conventional CP-PDD, the pole-pair number of stators P_{oc}, modulation ring Z_{mc}, and inner rotor P_{ic} meet (1). The speed ratio G_{rc} of the inner rotor and outer rotor meets (2). Due to the change of transmission structure, while keeping the pole-pair numbers of stator and inner rotor unchanged, the gear ratio changes in the proposed machine. The pole-pair numbers of stator P_o, outer rotor P_m, and inner rotor Z_i meet (3). The speed ratio G_r of the inner rotor and outer rotor meets (4) in the proposed machine.

$$Z_{mc} = P_{oc} + P_{ic} \tag{1}$$

$$G_{rc} = -\frac{\omega_{ic}}{\omega_{mc}} = -\frac{Z_{mc}}{P_{ic}} \tag{2}$$

$$P_o = P_m + Z_i \tag{3}$$

$$G_r = -\frac{\omega_i}{\omega_m} = \frac{P_m}{Z_i} \tag{4}$$

2.2. Working Principle

CP-PDD can be divided into two machines with rotor PMs or stator PMs in Fig. 2. When PMs in the stator are removed, the proposed machine can be regarded as a permanent magnet vernier machine (PMVM) [14]. When PMs in the rotor are removed, the machine can be regarded as a flux reversal machine (FRM). In addition, the MG generates torque on the inner rotor and outer rotor. The synthetic torque on the inner rotor is close to 0, and the output torque is a synthetic of the torque from PMVM, FRM, and MG. In PDD, the high-speed rotor is not connected to loads, while the low-speed rotor with low-speed high torque is connected to the mechanical load.

To simplify the calculation, the permeability of iron and the end effect are neglected. The air-gap flux density of each part of separated FSCP-PDD will be analyzed as follows. The initial positions of the inner rotor θ_{i0} and outer rotor θ_{o0} are set to zero to analyze the PMVM and FRM. The mechanical positions of the inner rotor θ_i and pole piece rotor θ_m can be calculated as (5) and (6)

$$\theta_i = \theta_{i0} + \omega_i t = \omega_i t \tag{5}$$

$$\theta_m = \theta_{m0} + \omega_m t = -\frac{Z_i}{P_m}\omega_i t \tag{6}$$

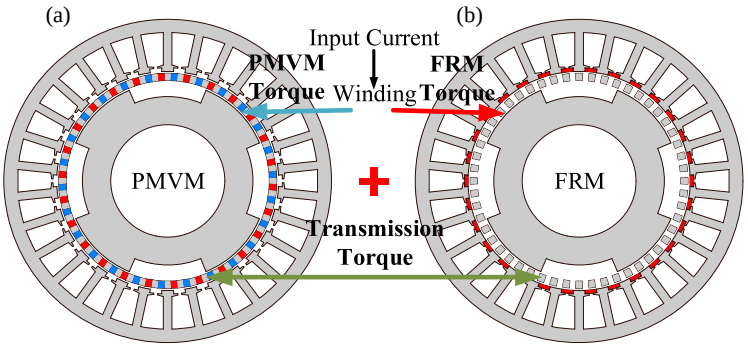

FIGURE 2. Principle of FSCP-PDD. (a) PMVM. (b) FRM.

where ω_i, ω_m, Z_i, and P_m are the angular velocities and pole-pair numbers of the inner rotor and pole piece rotor, respectively.

Firstly, the torque of PMVM is analyzed. When PMs in slot openings are removed, the proposed machine can be regarded as a PMVM. In [22], the magnetomotive force (MMF) of PMs can be expressed as

$$F_v(\theta,t) = \sum_{j=1,3}^{+\infty} \frac{8B_r\theta_{pm}r_g l_m \delta_{g'}}{j\pi\left(\mu_0\theta_{pm}\theta_p r_g^2 + 4\mu_0\mu_{rm}\delta_{g'}l_m\right)} \times \sin\left(\frac{j\pi}{2}\right)\cos\left(\frac{jP_m\theta_{pm}}{2}\right)\cos\left[jP_m(\theta-\omega_m t)\right] \quad (7)$$

where B_r is the remanence of PMs, θ_{pm} and θ_p are the angular widths of one pole of rotor PMs and iron, r_g the average radius of the air gap, l_m the radial length of rotor PMs, $\delta_{g'}$ the equivalent air-gap length, μ_0 the vacuum permeability, and μ_{rm} the relative permeability of PMs. The air gap of the machine is regarded as a double saliency structure because of the stator slots and inner rotor slots. The permeance function can be expressed as

$$\Lambda_v(\theta,t) \approx \frac{2\delta_g}{\mu_0}\Lambda_{vo}(\theta,t)\Lambda_{vi}(\theta-\theta_i,t) \quad (8)$$

where Λ_{vo} and Λ_{vi} are the permeance functions when only stator slots and inner rotor are considered. Λ_{vo} can be calculated as (9)–(13), where Λ_{v0} and Λ_{vk} are constant and the kth term in permeance function; Z_o is the number of stator teeth; θ_t and θ_s are the angular widths of stator tooth and stator slot; δ_g is the air-gap length, respectively. Similarly, Λ_{vi} can be calculated in the same way. Thus, the no-load air-gap flux density can be given by (14).

$$\Lambda_{vo}(\theta) = \Lambda_{v0} + \sum_{k=1,2}^{+\infty}\Lambda_{vk}\cos(kZ_o\theta) \quad (9)$$

$$\Lambda_{v0} = \frac{Z_o}{2\pi}\left(\Lambda_t\theta_t + \Lambda_s\theta_s\right) \quad (10)$$

$$\Lambda_{vk} = \frac{2(\Lambda_s-\Lambda_t)}{k\pi}\sin\left(\frac{kZ_o\theta_s}{2}\right) \quad (11)$$

$$\Lambda_t = \frac{\mu_0\theta_t r_g L_a}{\delta_g} \quad (12)$$

$$\Lambda_s = \frac{4\mu_0 L_a}{\pi}\ln\left(1+\frac{\pi\theta_s r_g}{4\delta_g}\right) \quad (13)$$

$$B_v(\theta,t) = F_v(\theta,t)\Lambda_v(\theta,t) \quad (14)$$

Then, the torque of FRM is analyzed. When PMs in the outer rotor are removed, the proposed machine can be regarded as an FRM. The MMF of stator PMs can be expressed as

$$F_f(\theta) = F_{f0} + \sum_{i=1,3}^{+\infty} F_{fi}\cos(iP_o\theta) \quad (15)$$

where F_{fi} is the ith term in MMF function. Due to the mechanical positions of rotors being determined by (5) and (6), the permeance of rotors can be simply taken into a single form. The air-gap permeance can be calculated as (16) where Λ_{f0} and Λ_{fj} are constant and the jth term in the permeance function. Thus, the no-load air-gap flux density can be given by (17).

$$\Lambda_f(\theta,t) = \frac{\mu_0}{2\delta_g + \Gamma(\theta,\theta_i) + \Gamma(\theta,\theta_m)} = \Lambda_{f0} + \sum_{j=1,2}^{+\infty}\Lambda_{fj}\cos\left[jP_m(\theta-\omega_m t)\right] \quad (16)$$

$$B_f(\theta,t) = \sum_{i=1,3}^{+\infty}\sum_{j=1,2}^{+\infty}\frac{F_{fi}\Lambda_{fj}}{2} \times \left\{\begin{array}{l}\cos[(iP_o+jP_m)\theta - jP_m\omega_m t] \\ -\cos[(iP_o-jP_m)\theta + jP_m\omega_m t]\end{array}\right\} + F_{f0}\Lambda_{f0} + F_{f0}\sum_{j=1,2}^{+\infty}\Lambda_{fj}\cos[jP_m(\theta-\omega_m t)] \quad (17)$$

The general expression of back EMF can be given as,

$$E = -\frac{d}{dt}\left[r_g L\int_0^{2\pi} B(\theta_s,t)N_w(\theta_s)d\theta_s\right] \quad (18)$$

where L is the stack length, and N_w is the winding function. The electromagnetic torque of PMVM and FRM can be calculated from (19) where $i_{a,b,c}$ is three phase instant current and I_m the amplitude of the current.

$$T = \frac{E_a i_a + E_b i_b + E_c i_c}{\omega_m} = \sum_{i=|6n\pm1|, n=0,1\ldots} 3E_i I_m/(2\omega_m)\cos\left[(i\mp1)P_r\omega_m t + \theta_i\right] \quad (19)$$

Then, both PMs in the outer rotor and inner rotor are reserved, and there is torque transmission between the two rotors. To facilitate the analysis of open-circuit air-gap flux density, a relative coordinate system is established on the outer rotor and expressed in (20).

$$\theta_{re} = \theta_m + \theta \quad (20)$$

Finally, the torque of FSMG is analyzed. As an FSMG, the magnetomotive force of the pole piece rotor is modulated by the permeance of pole pieces and teeth of the high-speed rotor. The magnetomotive force of the pole piece rotor is expressed as (7). The permeances of pole pieces and high-speed rotor are expressed as

$$\Lambda_m = \Lambda_{m0} + \Lambda_{ma}\cos(P_m\theta_{re}) \quad (21)$$

$$\begin{aligned}\Lambda_i &= \Lambda_{i0} + \Lambda_{ia}\cos(Z_i\theta_{im} - Z_i\omega_{im}t) \\ &= \Lambda_{i0} + \Lambda_{ia}\cos\left(Z_i\theta_{re} - Z_i\omega_{im}t - Z_{im}\delta_{im}\right)\end{aligned} \quad (22)$$

where Λ_{m0}, Λ_{ma}, Λ_{i0}, Λ_{ia}, Λ_{im}, Λ_{im}, and Λ_{im} are the average component of the permeance of the pole pieces, the amplitude of the permeance of the pole pieces, the average component of the permeance of the high-speed rotor, the amplitude of the permeance of the high-speed rotor, the mechanical angle of the inner rotor relative to the pole piece rotor, the angular speed of the inner rotor relative to the pole piece rotor, and the deviation angle between the center of pole pieces and the center of the high-speed rotor, respectively. Then, the flux distribution in the air gap is obtained as,

$$\begin{aligned}B_{mg}(\theta_{re},t) &= F_{va}\Lambda_{i0}\Lambda_{m0}\cos(P_m\theta_{re}) + \frac{1}{2}F_{va}\Lambda_{i0}\Lambda_{ma} \\ &\{\cos\left[(P_m+Z_i)\theta_{re}\right] + \cos\left[(P_m-Z_i)\theta_{re}\right]\} \\ &+\frac{1}{2}F_{va}\Lambda_{m0}\Lambda_{ia} \\ &\left\{\begin{array}{l}\cos\left[(P_m+Z_i)\theta_{re} - Z_i(\omega_{im}t+\delta_{im})\right] \\ +\cos\left[(P_m-Z_i)\theta_{re} + Z_i(\omega_{im}t+\delta_{im})\right]\end{array}\right\} \\ &+\frac{1}{4}F_{va}\Lambda_{ma}\Lambda_{ia} \\ &\left\{\begin{array}{l}\cos\left[(P_m+P_o+Z_i)\theta_{re} - Z_i(\omega_{im}t+\delta_{im})\right] \\ +\cos\left[(P_m-P_o-Z_i)\theta_{re} + Z_i(\omega_{im}t+\delta_{im})\right] \\ +\cos\left[(P_m+P_o-Z_i)\theta_{re} + Z_i(\omega_{im}t+\delta_{im})\right] \\ +\cos\left[(P_m-P_o+Z_i)\theta_{re} - Z_i(\omega_{im}t+\delta_{im})\right]\end{array}\right\}\end{aligned} \quad (23)$$

As shown in (23), the fourth term and fifth term of (23) contribute to the magnetic coupling. Then, the average torque is expressed as

$$T = \frac{\partial W_m}{\partial\theta} = \frac{1}{2\pi}\int_0^{2\pi} B\times\frac{\partial F}{\partial\theta}d\theta \quad (24)$$

where T, W_m, and F are the average torque, magnetic energy, and magnetomotive force, respectively. Thus, the torque equations of the high-speed rotor and low-speed rotor are expressed as (25) and (26). The output torque from the low-speed rotor is the sum of the torque of FSMG and the electromagnetic torque of the PMVM and FRM.

$$\begin{aligned}T_i &= \frac{1}{4}F_{oa}F_{ma}\Lambda_{m0}\Lambda_{ia}Z_i \\ &\times\sin\left[(-P_o\omega_{om}\pm Z_i\omega_{im})t - P_o\delta_{om}\pm Z_i\delta_{im}\right]\end{aligned} \quad (25)$$

$$\begin{aligned}T_m &= \frac{1}{4}F_{oa}F_{ma}\Lambda_{m0}\Lambda_{ia}P_m \\ &\times\sin\left[(-P_o\omega_{om}\pm Z_i\omega_{im})t - P_o\delta_{om}\pm Z_i\delta_{im}\right]\end{aligned} \quad (26)$$

3. PARAMETRIC OPTIMIZATION

To achieve higher output torque and lower torque ripple, the key parameters will be analyzed and optimized through a multi-objective genetic algorithm (MOGA) method [23]. Before optimization, the influence of some leading parameters on the torque density and torque ripple will be analyzed for design guidelines of the proposed FSCP-PDD machine [24]. When optimizing parameters, the total volume, current density, axial length, outer radius, etc. will be kept unchanged. A full parametric model of the proposed machine is established in Fig. 3.

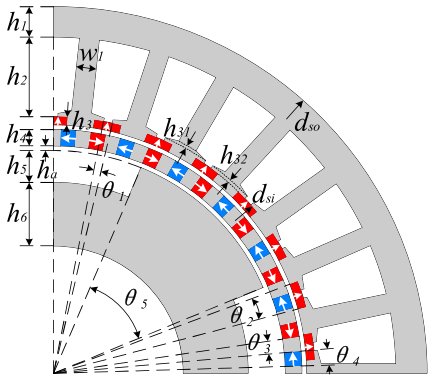

FIGURE 3. Design parameters of the full parameterized model.

3.1. Number of Stator Teeth

The influence of stator teeth number on transmission ratio (TR) and torque density is shown in Table 1. With the change of stator tooth number and pole-pair number of stator PM P_o, the winding factor, pole-pair number of outer rotor P_m, and TR of MG change correspondingly. The torque performances of the machine with the number of stator teeth of 18, 30, and 42 are compared under the premise of keeping the current density, cross-sectional area of slots, total turns of winding, and volume of PM unchanged. As can be seen from Table 1, with

TABLE 1. Influence of stator teeth number on the average torque.

P_o	P_m	TR	Winding step	Winding factor	Output torque (N·m)
18	14	3.5	2	0.945	181.65
30	26	6.5	4	0.951	213.87
42	38	9.5	5	0.953	196.90

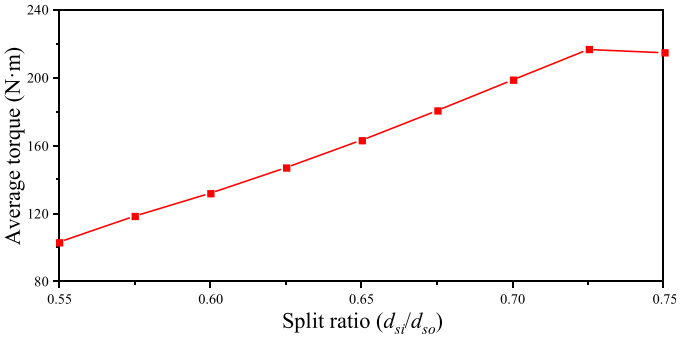

FIGURE 4. Influence of split ratio on the average output torque.

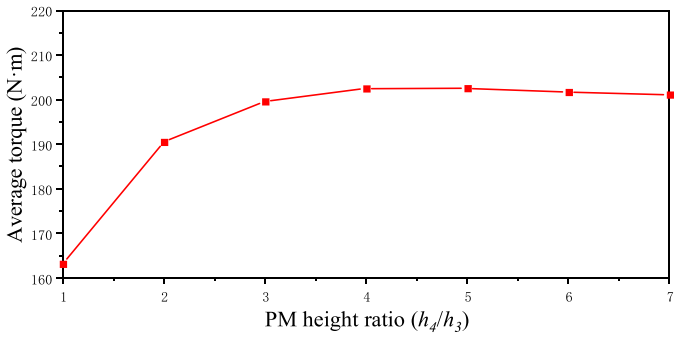

FIGURE 5. Influence of PM height ratio on the average output torque.

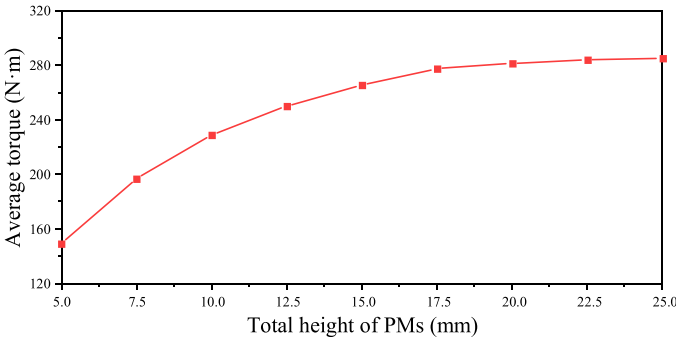

FIGURE 6. Influence of total height ratio on the average output torque.

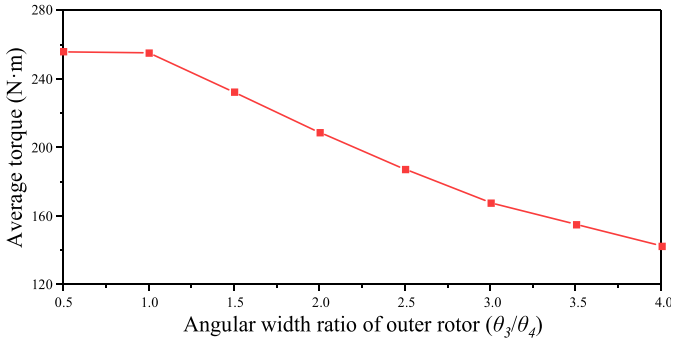

FIGURE 7. Influence of angular width ratio of the outer rotor on the average torque.

the increase of the stator teeth number, the output torque of the machine will increase and then decrease. An increase in the number of pole pairs also leads to an increase in loss and a decrease in efficiency [25]. Thus, the model with 30 stator teeth is selected for further optimization and study.

3.2. Split Ratio

The influence of the split ratio on the output torque and torque ripple is shown in Fig. 4. The more the split ratio is, the more the space of the PM and armature winding is, and the less the equivalent air-gap radius is. However, when the split ratio is much too high with serious magnetic saturation, the average torque will decrease. Some margin is preserved to prevent the occurrence of magnetic saturation while the maximum average torque is obtained when the split ratio is selected as 0.7.

3.3. PM Dimension

Figure 5 shows the effect of the ratio of rotor PM height to stator PM height on average torque. The influence of the total height of PM on average torque is shown in Fig. 6. The influence of the shape and size of PMs on the average torque is analyzed when the outer diameter and split ratio are determined. When the total volume of PMs is fixed, the larger the volume of the rotor PM is, the higher the torque generated by the PMVM is. At the same time, the volume of stator PM and rotor PM will affect the transmission torque of MG. The higher the total height of the PM is, the greater the average torque of the machine is, but the height of the PM is not linearly related to the volume of PM. The torque of the machine with an excessive height of PM will decrease due to flux leakage, magnetic saturation, and narrowing of the inner rotor space.

The influence of the angular width ratio of the outer rotor core to the outer rotor PM on the average torque is shown in Fig. 7. With the decrease of the ratio, the PM volume increases, but the volume of pole pieces with the function of flux modulation decreases, and the average torque increases first and then slows down. The influence of the angular width of stator PM on average torque is shown in Fig. 8. The angular width of stator PM also determines the angular width of stator teeth on the side of PM.

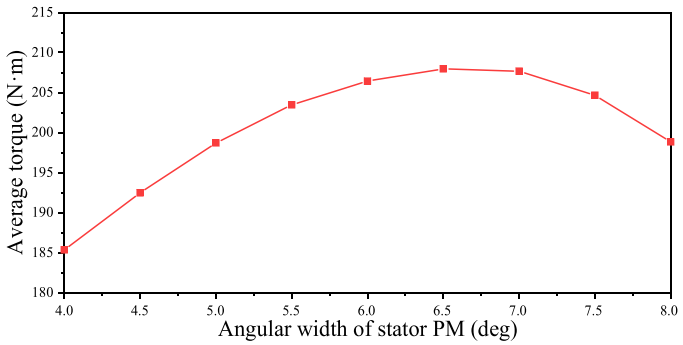

FIGURE 8. Influence of angular width of stator PM on the average output torque.

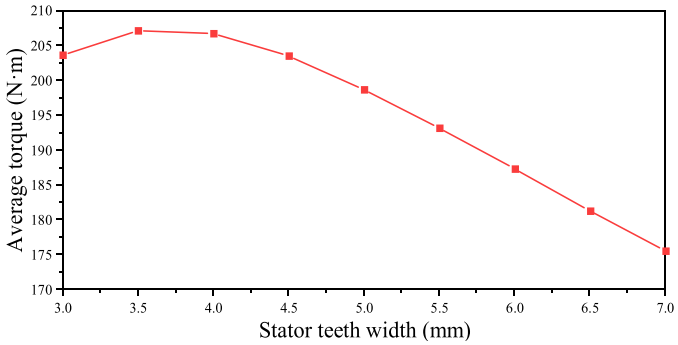

FIGURE 9. Influence of stator teeth width on the average output torque.

As a trade-off, the optimal values of the above four parameters for the proposed machine should be selected as 3.5, 10 mm, 2.5, and 5 deg respectively.

3.4. Stator and Rotor Teeth

The influence of stator teeth width on the average torque of the proposed machine is shown in Fig. 9. The narrower the stator teeth are, the more space is left for the winding, and the higher the armature winding current and output torque are when the current density is fixed. However, the narrower the stator teeth are, the less flux can pass through them. Some margin is preserved to prevent magnetic saturation while the optimal stator teeth width for the proposed machine is selected as 5 mm. Under this parameter, the motor exhibits high average torque, high utilization rate of permanent magnets, low loss, and relatively low operating temperature.

The influence of inner rotor teeth height on the average torque of the proposed FSCP-PDD machine is shown in Fig. 10. The height of rotor teeth will influence both the output torque and the torque on the inner rotor. The torque of the inner rotor increases with the increase of the rotor teeth height, while the output torque decreases with the increase of the rotor teeth height. The optimal rotor teeth height for the proposed machine should be selected depending on the specific design requirements so that the torque on the inner rotor is 0.

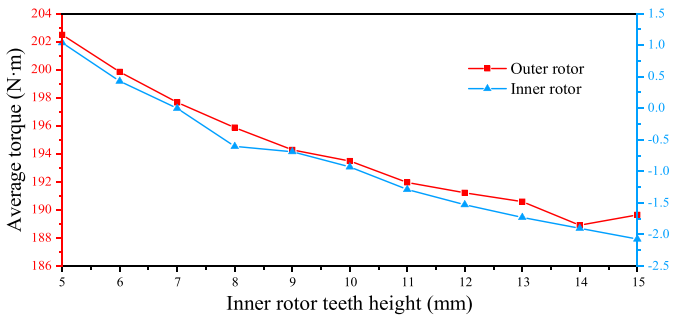

FIGURE 10. Influence of inner rotor teeth height on the average output torque.

3.5. Global Optimization

The method of single-parameter scanning determines the influence of design parameters. Meanwhile, it selects the parameters that have significant influence on the optimization results for MOGA optimization. The above individual parametric optimizations provide guidelines for global optimization. Considering the copper loss, iron loss, and PM eddy current loss at 300 r/min for the outer rotor and 1950 r/min for the inner rotor of the proposed machine, the objective functions of maximum average torque, minimum torque ripple, and maximum torque per unit PM volume are given, while the temperature of the winding and PM is roughly set at 100°C. Fig. 11 shows the Pareto front of MOGA, which best meets the requirements of output torque as large as possible and torque ripple as small as possible. The optimized parametric values are shown in Table 2. Under the premise that the main parameters such as PM volume, outer diameter, and stack length are unchanged, the conventional CP-PDD is optimized and shown in Table 2 as well.

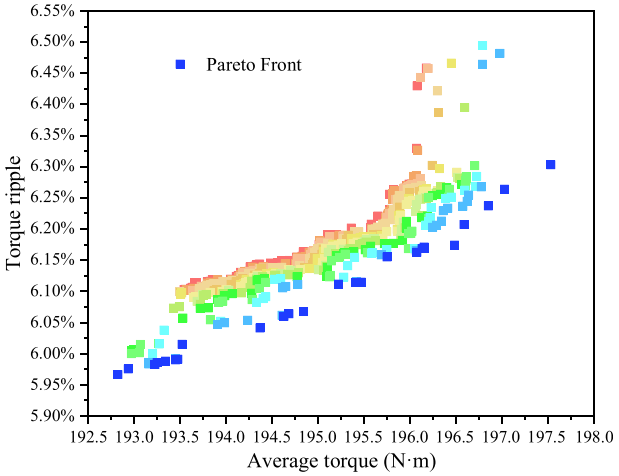

FIGURE 11. Pareto front of MOGA.

4. PERFORMANCE COMPARISON AND ANALYSIS

The open-circuit radial flux density of the proposed machine and harmonics spectra comparison of the outer air gap are shown in Fig. 12. It can be seen from Fig. 12(b) that the open-circuit flux density harmonics of the outer air gap of the conventional CP-PDD are mainly the 4th and 30th, while the flux density harmonics of the proposed FSCP-PDD are mainly the 26th and 30th harmonics. In the conventional CP-PDD, the 4th

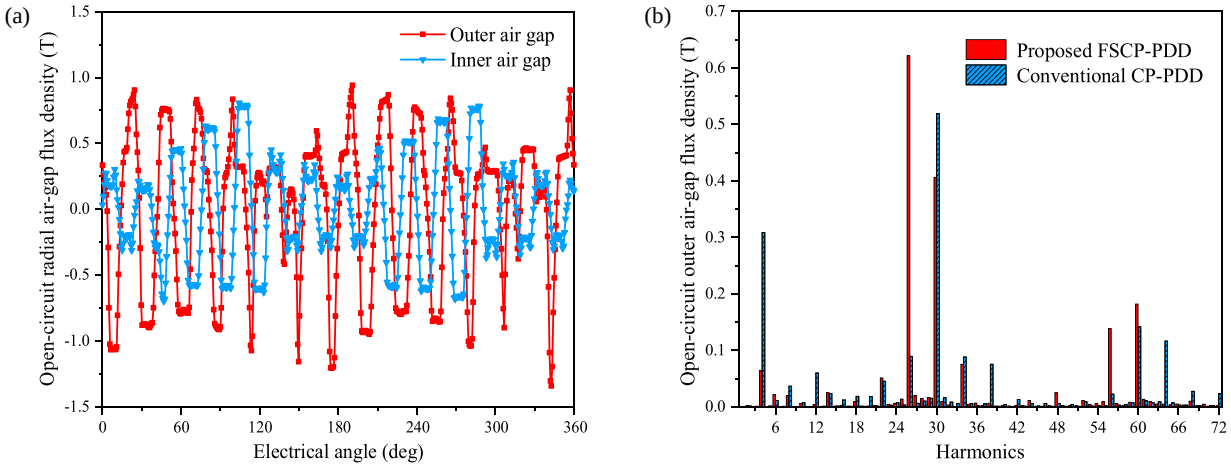

FIGURE 12. Flux density. (a) Flux density distribution of proposed machine. (b) Outer air-gap harmonics spectra comparison.

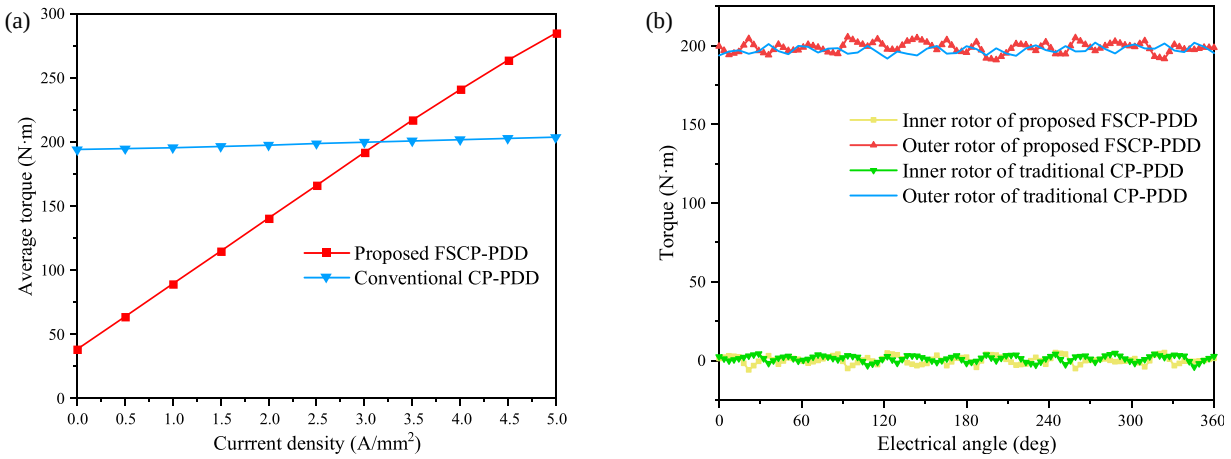

FIGURE 13. Output torque. (a) Average torque at different current densities. (b) Transient torque at rated speed and current density.

harmonic of the outer air-gap flux density mainly produces EM torque, driving the inner rotor rotation. In the proposed FSCP-PDD, the 26th harmonic in the outer air-gap flux density is modulated by 30 stator teeth to generate the EM torque of PMVM.

The average output torque comparison of the proposed and conventional machines at different current densities is shown in Fig. 13(a). The torque performance of the FSMG is much lower than that of the conventional MG, but the contribution of the EM torque to the output torque in the proposed machine is much higher than that of the conventional CP-PDD. The EM torque of CP-PDD is mainly generated on the high-speed rotor and transmitted by the MG. When the current density is 3.2 A/mm^2, the output torque of the proposed machine is equal to that of the conventional machine. The transient torque comparison of the two machines is shown in Fig. 13(b). In the process of optimization, the slot area, winding turns, outer radius, PM volume, and stack length of the two machines are set to the same to facilitate comparison. Torques of them on the inner rotor are 0 at rated current densities.

The loss comparison between the proposed machine and conventional machine in each region at rated current density and different speeds is shown in Fig. 14. With the increase in speed, the loss of the conventional machine increases more than that of the proposed machine. The loss of the conventional machine is mainly composed of the eddy current loss of stator PM, while the loss of the proposed machine is mainly composed of the eddy current loss of stator PM and rotor PM.

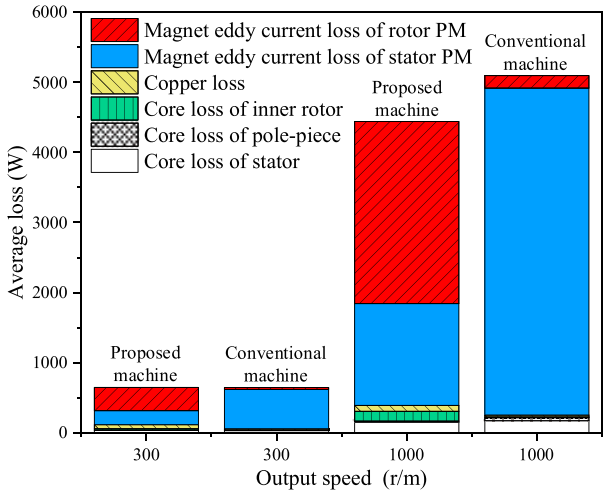

FIGURE 14. Loss comparison between the proposed and conventional machines at different output speeds.

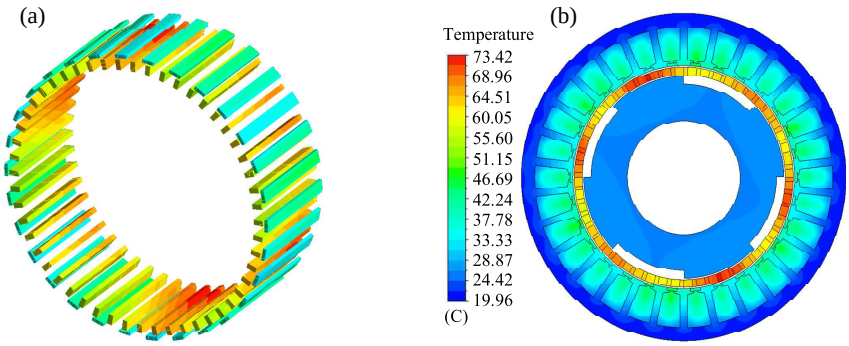

FIGURE 15. Temperature of the proposed machine at rated speed. (a) PMs. (b) Cross section of the proposed machine.

TABLE 2. Main parameters of the proposed FSCP-PDD and conventional CP-PDD after optimization.

Parameters	FSCP-PDD	CP-PDD
Stator tooth number	30	
Pole-pair number of pole piece rotor	26	34
Inner rotor pole number	4	
Outer radius (mm)	115	
Stack length (mm)	60	
Air-gap length h_a (mm)	1	
Split ratio	0.7	
Stator yoke height h_1 (mm)	9.50	
Slot height h_2 (mm)	25	
Outer PM height h_3 (mm)	1.97	2.03
h_{31} (mm)	1	
h_{32} (mm)	1	
Pole piece height h_4 (mm)	5.65	8.76
Rotor tooth height h_5 (mm)	6.5	2.67
Inner radius (mm)	40	
Stator tooth width w_1 (mm)	5	
Slot opening angular width θ_1 (deg)	2	
Outer PM angular width θ_2 (deg)	5	7.93
Pole piece angular width θ_3 (deg)	4.75	5.29
Inner PM angular width θ_4 (deg)	2.17	46.88
Rotor tooth angular width θ_5 (deg)	44.62	43.12
Turns per phase	400	
Steel material	DW540-50	
PMs material	N40UH	
Slot fill	0.45	

The temperature distribution of the proposed machine with rated speed considering the thermal magnetic coupling and the axial wind speed of 34.1 m/s in the air gap inlet is shown in Fig. 15. Natural heat dissipation cannot meet the heat dissipation requirements. Therefore, the proposed machine needs to adopt air-cooling heat dissipation. It can be seen from Fig. 15(a) that at the rated speed, the maximum temperature of the PM as the main heat source is 73°, which is much lower than the maximum operating temperature of N40UH. Fig. 15(b) intercepts the cross-section of the highest temperature area inside the proposed machine, and all parts of the machine are within the permissible operating temperature range.

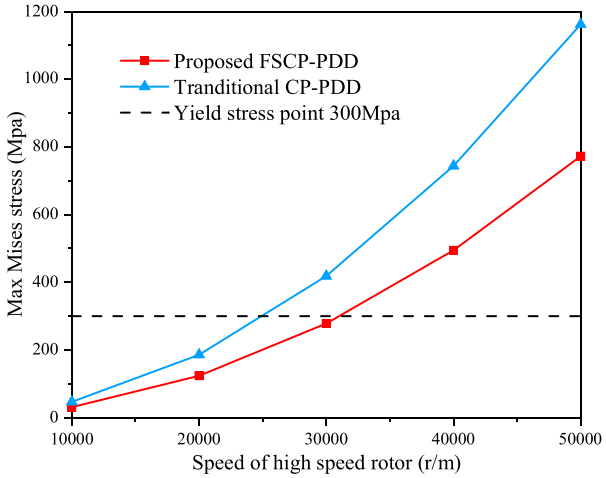

FIGURE 16. Max Mises stress of high-speed rotor.

The maximum Mises stress comparison between the proposed machine and conventional machine at different speeds is shown in Fig. 16. The faster the rotation speed is, the greater the shear force caused by the rotation of the rotor is, so only the Mises stress of the high-speed rotor should be considered. Considering that the yield stress is 300 MPa, the speed of the inner rotor of CP-PDD should be lower than 25000 r/m, while the speed of FSCP-PDD can reach 30000 r/m. When the speed of the high-speed rotor is 25000 r/m, the Mises stress comparison between the conventional CP-PDD machine and the proposed FSCP-PDD machine is shown in Fig. 17. The maximum Mises stress of FSCP-PDD is smaller than that of CP-PDD, and the mechanical strength is stronger, which is more suitable for high-speed driving.

5. EXPERIMENTS

To further verify the performance of the proposed machine and validate the FEA simulations, a prototype is fabricated, and an experimental platform is built as shown in Fig. 18. The output rotor of the proposed machine is connected to a magnetic particle brake through a 500 N·m torque transducer while the inner rotor of the proposed machine is idling. To ensure the safety of the prototype trial, the test speed and torque of the rotor are

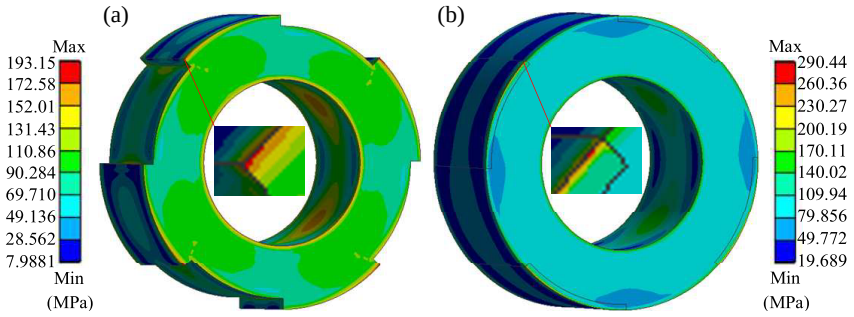

FIGURE 17. Mises stress comparison of the high-speed rotor at 25000 r/m. (a) FSCP-PDD. (b) CP-PDD.

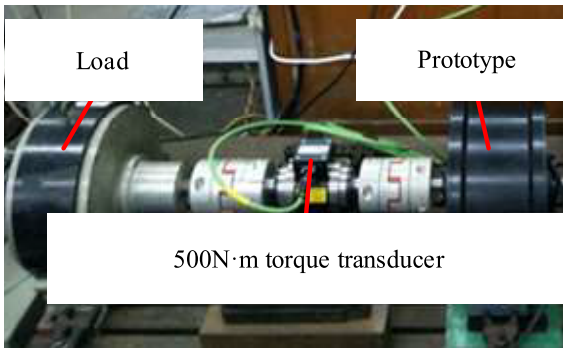

FIGURE 18. Prototype and experiment bench.

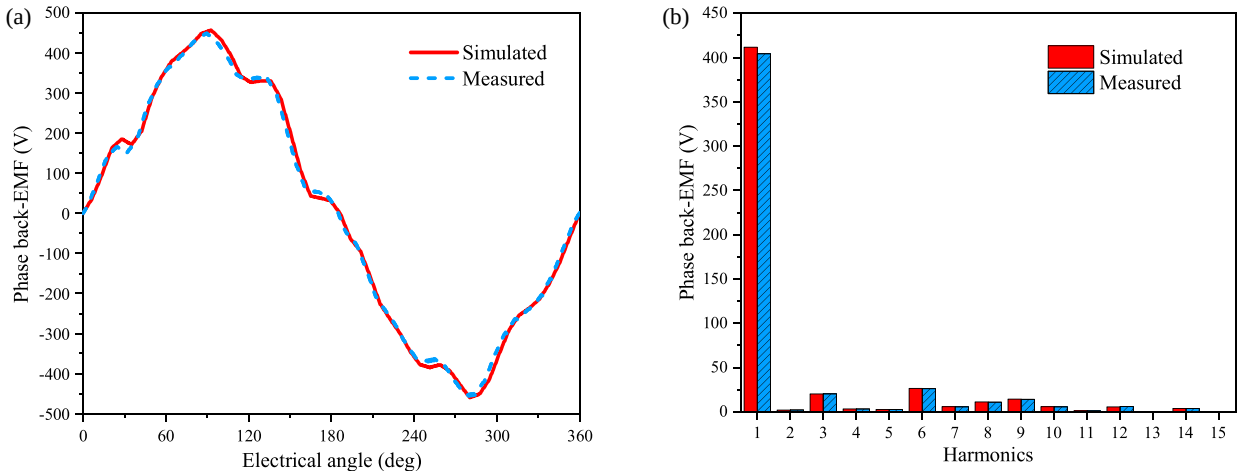

FIGURE 19. Back-EMF of the proposed machine. (a) The waveform of back-EMF. (b) Harmonics spectra.

lower than the maximum speed and torque determined by the FEM.

5.1. Open-Circuit Experiment

The open-circuit phase back-EMFs and harmonics spectra at rated speed are measured and shown in Fig. 19. The simulated results considering loss and temperature are compared with the measurement. It is noticed that small amounts of high-order harmonics occur in the back-EMF of the proposed machine. The poor sinusoidal of the back-EMF will lead to harmonic EM torque and other shortcomings, but the output torque ripple is relatively low when the EM torque is combined with the transmission torque of the MG. It is observed that there is a basic agreement between the simulated and measured results while the amplitude of measurement is slightly smaller than simulated results. The main factors causing the difference may be the error in PM temperature and the number of PMs. However, the difference is within the acceptable range.

5.2. Load Experiment

Furthermore, the load experiment is conducted before pull-out. The measured and simulated torques under rated current are

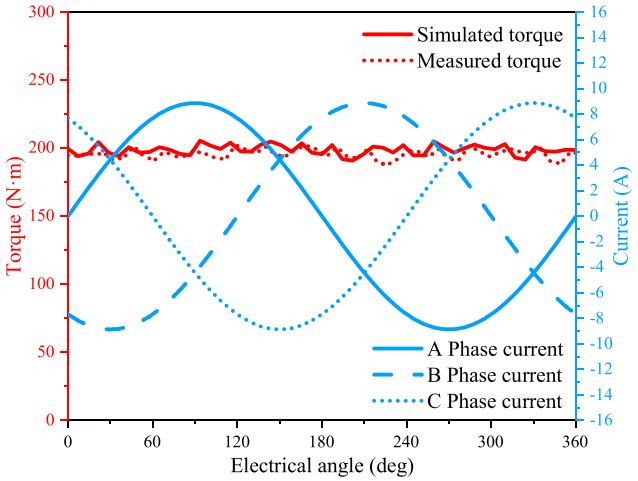

FIGURE 20. Measured and simulated torques under rated current.

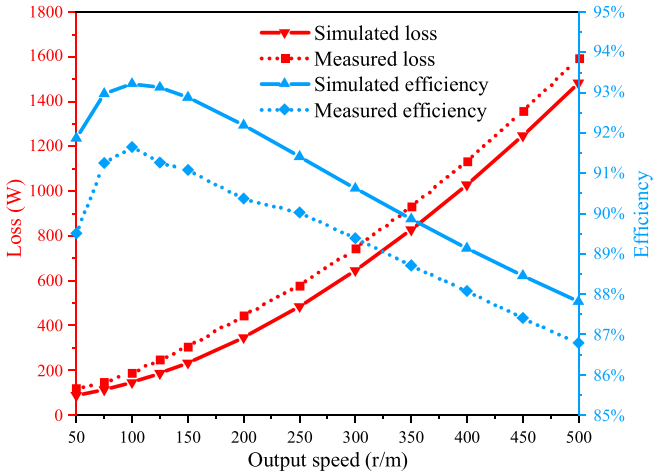

FIGURE 21. Measured and simulated losses and efficiencies at different speeds.

shown in Fig. 20. It is observed that there is a basic agreement between the simulated and measured results while the average torque of measurement is slightly smaller than simulated results. The difference of phase back-EMF causes the difference in torque. However, the difference is within the acceptable range.

The loss and efficiency at different speeds are shown in Fig. 21. The simulated loss mainly includes magnet eddy current loss of PMs, iron loss, and DC and AC components of copper loss. Compared with the measured loss of the prototype, the simulated loss does not consider mechanical friction loss, wind friction loss, etc. Due to the certain deviation in the processing of the prototype and the difference in considered loss, the simulated performance of loss and efficiency is slightly worse than the measured results. However, the error is acceptable. The performances of the proposed machine are shown in Table 3.

TABLE 3. Performances of proposed machine.

Item	Value
Current density (A/mm^2)	3.2
Average rated torque (N·m)	194.1
Torque ripple	6.5%

6. CONCLUSION

This paper proposes a novel FSCP-PDD machine that is more suitable for high-speed driving. Concerning FSMG, the rotor PM of the conventional CP-PDD machine is moved from the inner rotor to the outer rotor, which changes the working principle of the machine. After optimizing the CP-PDD machine and FSCP-PDD machine by MOGA, the EM properties are compared and analyzed. The output torque density of FSMG is lower than that of conventional MG, but due to the presence of direct drive torque, the FSCP-PDD machine has higher design freedom than the CP-PDD machine. A prototype is built and tested to verify the proposed machine. Under the same output torque, the FSCP-PDD machine has less loss than the CP-PDD machine with high-speed driving, and the high-speed rotor of the proposed machine has better robustness. It has been proved that under suitable air-cooling conditions, the operating temperature of the FSCP-PDD machine is within a reasonable range.

REFERENCES

[1] Zhu, X. and W. Hua, "Stator-slot/rotor-pole pair combinations of flux-reversal permanent magnet machine," *IEEE Transactions on Industrial Electronics*, Vol. 66, No. 9, 6799–6810, Sep. 2019.

[2] Cheng, M., P. Han, and W. Hua, "General airgap field modulation theory for electrical machines," *IEEE Transactions on Industrial Electronics*, Vol. 64, No. 8, 6063–6074, Aug. 2017.

[3] Fang, L., D. Li, and R. Qu, "Torque improvement of vernier permanent magnet machine with larger rotor pole pairs than stator teeth number," *IEEE Transactions on Industrial Electronics*, Vol. 70, No. 12, 12 648–12 659, Dec. 2023.

[4] Atallah, K. and D. Howe, "A novel high-performance magnetic gear," *IEEE Transactions on Magnetics*, Vol. 37, No. 4, 2844–2846, Jul. 2001.

[5] Kashani, S. A. A., "Design and optimization of coaxial reluctance magnetic gear with different rotor topologies," *IEEE Transactions on Industrial Electronics*, Vol. 69, No. 1, 101–109, Jan. 2022.

[6] Wang, Y., M. Filippini, N. Bianchi, and P. Alotto, "A review on magnetic gears: Topologies, computational models, and design aspects," *IEEE Transactions on Industry Applications*, Vol. 55, No. 5, 4557–4566, Sep.–Oct. 2019.

[7] Jing, L., W. Liu, W. Tang, and R. Qu, "Design and optimization of coaxial magnetic gear with double-layer PMs and spoke structure for tidal power generation," *IEEE/ASME Transactions on Mechatronics*, Vol. 28, No. 6, 3263–3271, 2023.

[8] Atallah, K., J. Rens, S. Mezani, and D. Howe, "A novel 'pseudo' direct-drive brushless permanent magnet machine," *IEEE Transactions on Magnetics*, Vol. 44, No. 11, 4349–4352, Nov. 2008.

[9] Cooke, G. and K. Atallah, "Pseudo direct drive electrical machines with alternative winding configurations," *IEEE Transactions on Magnetics*, Vol. 53, No. 11, 1–8, Nov. 2017.

[10] Gerber, S. and R.-J. Wang, "Design and evaluation of a magnetically geared PM machine," *IEEE Transactions on Magnetics*, Vol. 51, No. 8, 1–10, Aug. 2015.

[11] Dragan, R. S., R. E. Clark, E. K. Hussain, K. Atallah, and M. Odavic, "Magnetically geared pseudo direct drive for safety critical applications," *IEEE Transactions on Industry Applications*, Vol. 55, No. 2, 1239–1249, Mar.–Apr. 2019.

[12] Niguchi, N. and K. Hirata, "Magnetic-geared motors with high transmission torque density," *COMPEL*, Vol. 34, No. 2, 428–438, 2015.

[13] Niguchi, N., K. Hirata, E. Morimoto, and Y. Ohno, "Magnetizing directions of the permanent magnets of the magnetic-geared motor," in *2014 International Conference on Electrical Machines (ICEM)*, 1279–1285, Berlin, Germany, Sep. 2014.

[14] Huang, H., D. Li, W. Kong, and R. Qu, "Torque performance of pseudo direct-drive machine with Halbach consequent pole," in *2018 IEEE Energy Conversion Congress and Exposition (ECCE)*, 3286–3293, Portland, OR, USA, 2018.

[15] Gan, Q., Y. Fang, and P.-D. Pfister, "A novel concentrated-winding vernier pseudo-direct-drive permanent-magnet machine," *IEEE Transactions on Magnetics*, Vol. 58, No. 2, 1–5, Feb. 2022.

[16] Aiso, K., K. Akatsu, and Y. Aoyama, "A novel flux-switching magnetic gear for high-speed motor drive system," *IEEE Transactions on Industrial Electronics*, Vol. 68, No. 6, 4727–4736, Jun. 2021.

[17] Traxler-Samek, G., R. Zickermann, and A. Schwery, "Cooling airflow, losses, and temperatures in large air-cooled synchronous machines," *IEEE Transactions on Industrial Electronics*, Vol. 57, No. 1, 172–180, Jan. 2010.

[18] Wang, L., Y. Li, B. Kou, F. Marignetti, and A. Boglietti, "Influence of ventilation modes on the 3D global heat transfer of PMSM based on polyhedral mesh," *IEEE Transactions on Energy Conversion*, Vol. 37, No. 2, 1455–1466, Jun. 2022.

[19] Kim, H., H.-S. Jung, and S.-K. Sul, "Stator winding temperature and magnet temperature estimation of IPMSM based on high-frequency voltage signal injection," *IEEE Transactions on Industrial Electronics*, Vol. 70, No. 3, 2296–2306, Mar. 2023.

[20] Di Nardo, M., G. Gallicchio, M. Palmieri, A. Marfoli, G. L. Calzo, M. Degano, C. Gerada, and F. Cupertino, "High-speed synchronous reluctance machines: Materials selection and performance boundaries," *IEEE Transactions on Transportation Electrification*, Vol. 8, No. 1, 1228–1241, Mar. 2022.

[21] Wang, C., J. Han, Z. Zhang, Y. Hua, and H. Gao, "Design and optimization analysis of coreless stator axial-flux permanent magnet in-wheel motor for unmanned ground vehicle," *IEEE Transactions on Transportation Electrification*, Vol. 8, No. 1, 1053–1062, Mar. 2022.

[22] Li, X., K. T. Chau, M. Cheng, B. Kim, and R. D. Lorenz, "Performance analysis of a flux-concentrating field-modulated permanent-magnet machine for direct-drive applications," *IEEE Transactions on Magnetics*, Vol. 51, No. 5, 1–11, May 2015.

[23] Fan, D., X. Zhu, L. Quan, P. Han, Z. Xiang, and J. Wu, "Driving cycle design optimization of less-rare-earth PM motor using dimension reduction method," *IEEE Transactions on Energy Conversion*, Vol. 38, No. 3, 1614–1625, Sep. 2023.

[24] Cai, S., H. Chen, X. Yuan, Y.-C. Wang, J.-X. Shen, and C. H. T. Lee, "Analysis of synergistic stator permanent magnet machine with the synergies of flux-switching and flux-reversal effects," *IEEE Transactions on Industrial Electronics*, Vol. 69, No. 12, 12 237–12 248, Dec. 2022.

[25] Zhao, Y., X. Ren, X. Fan, D. Li, and R. Qu, "A high power factor permanent magnet vernier machine with modular stator and yokeless rotor," *IEEE Transactions on Industrial Electronics*, Vol. 70, No. 7, 7141–7152, Jul. 2023.